JOURNAL OF SYNCHROTRON RADIATION
ISSN 1600-5775

Local strain and defects in silicon wafers due to nanoindentation revealed by full-field X-ray microdiffraction imaging

Z. J. Li,[a]* A. N. Danilewsky,[b] L. Helfen,[a] P. Mikulik,[c] D. Haenschke,[a] J. Wittge,[b] D. Allen,[d] P. McNally[d] and T. Baumbach[a]

[a]Institute for Photon Science and Synchrotron Radiation, Karlsruhe Institute of Technology, Germany, [b]Crystallography, University of Freiburg, Germany, [c]Institute of Condensed Matter Physics, Masaryk University, Czech Republic, and [d]School of Electronic Engineering, Dublin City University, Ireland.
*Correspondence e-mail: li.zhijuan@hotmail.com

Received 9 November 2014
Accepted 19 May 2015

Edited by G. E. Ice, Oak Ridge National Laboratory, USA

Keywords: XMDI; nanoindentation; silicon; strain; defect.

Quantitative characterization of local strain in silicon wafers is critical in view of issues such as wafer handling during manufacturing and strain engineering. In this work, full-field X-ray microdiffraction imaging using synchrotron radiation is employed to investigate the long-range distribution of strain fields in silicon wafers induced by indents under different conditions in order to simulate wafer fabrication damage. The technique provides a detailed quantitative mapping of strain and defect characterization at the micrometer spatial resolution and holds some advantages over conventional methods.

1. Introduction

Silicon has practical importance in nanoelectronics, microelectronics and micromechanics, as well as important optoelectronic materials and as a template for material synthesis. The use of high-quality silicon wafers is crucial for the fabrication of these and other microdevices. Over the past decades, high-quality silicon wafers have become the industry standard and the ultra-large-scale integration of microelectronics has developed dramatically. The continued geometric downscaling of devices on a chip will soon reach a physical limit, and in this situation strain and various defects have become a greater concern (Bouhassoune & Schindlmayr, 2010). Global and local strains in silicon can change dramatically the electronic, optical and mechanical properties (Gilman, 2008). Most strain induces damage and structural defects which leads to poor performance for the devices and in some cases can then even lead to wafer breakage. In contrast to its disadvantages, the use of appropriately strained silicon devices can push performance for nodes below 65 nm. The strain-induced linear electro-optic effect may be useful to remove a bottleneck in modern computers by replacing the electronics bus with a much faster optical alternative (Jacobsen *et al.*, 2006). However, wafer handling in semiconductor manufacturing can also introduce damage at the wafer edge if the tool is misaligned and during processing some of the micro-cracks appear to grow, resulting in wafer breakage and substantial disruption to the manufacturing process; plastic deformations are generated in a series of steps. These deformations are correlated with external and internal strains. It is critical to develop a metrology to predict the probability of catastrophic failure during processing of silicon wafers.

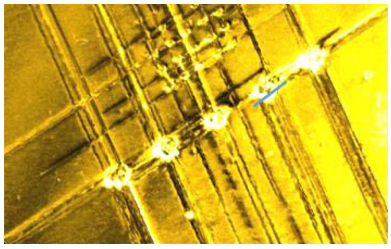

Nanoindentation is a variety of indentation hardness tests applied to small volumes. It uses small loads and tip sizes with an indent area of a few square micrometers or even nanometers. Nanoindentation in silicon (contact load) is an efficient method to simulate and investigate the mechanical processing and strain-related failure mechanisms (Domnich & Gogotsi, 2002). Different types of indenter can be applied for nanoindentation depending on the geometry of indentation and load. The Berkovich indenter is a three-sided type, with an angle of 65.03° between two side planes. The Vickers indenter is a four-sided type, with the angle between the side planes of 68°, and is generally applied to large indent loads.

Previous results have shown that a Si crystal near an indent undergoes a series of phase transitions depending on loading, unloading, loading speed of the indenter and heat treatment. Cross-sectional transmission electron microscopy and Raman microscopy (Tachi *et al.*, 2002; Ericson *et al.*, 1988) indicated an indentation-induced amorphization, recrystallization, generation of dislocations and cracks. Various phase transitions occur underneath the indenter tip where the highest plastic strains appear. These pressure- and indentation-induced phase transitions in crystalline materials have also been studied by using molecular dynamics simulations and finite-element modeling (FEM) (Khayyat *et al.*, 2003; Ivashchenko *et al.*, 2008). However, none of these techniques gives quantitative experimental evidence concerning the strain field over a long-range scale and they do not possess bulk probe capability either. X-ray topography provides a direct visualization of crystal defects (Danilewsky *et al.*, 2010); however, it lacks quantitative characterization capability. In this work, we report the investigation of local strain fields in silicon wafers induced *via* nanoindentation by means of the full-field X-ray microdiffraction imaging (XMDI) method using synchrotron radiation. XMDI has been developed to map the structural properties of crystalline samples and to assess the local lattice misorientations and deformations over a large sample area (Lübbert *et al.*, 2000; Mikulik *et al.*, 2003; Lübbert, Baumbach *et al.*, 2005; Lübbert, Ferrari *et al.* 2005). It can quantitatively assess local strain over a large sample area (several mm^2) with high-angular and spatial resolutions by combining X-ray diffraction with micrometer-scale spatial resolution imaging. The method is also called rocking-curve imaging.

2. Experimental

Silicon samples of size 2 cm × 2 cm and 750 µm thickness were cut from a whole piece of silicon wafer with (001) surface. An array of indents from 100 to 600 mN loads were made on as-received silicon wafers using a Berkovich indenter. Indents at 2 N were made using a Vickers indenter. An indented sample was further treated by slowly annealing at 1273 K. XMDI measurements were carried out at room temperature at beamline ID19 of the European Synchrotron Radiation Facility (ESRF) using a diffractometer situated at approximately 145 m from the source. A double Si (111) crystal monochromator was installed at the beamline to provide monochromatic radiation beams. The large source-to-sample distance has the advantage of allowing one to obtain a large homogeneous field-of-view with a very low angular beam divergence. The diffractometer was initially designed for laminography and tomography experiments (Helfen *et al.*, 2006). The samples were measured at 004 diffraction in Bragg reflection mode and 220 diffraction in transmission mode at 19 and 23.4 keV, respectively. A CCD camera (Frelon, 0.76 µm pixel size, 2048 × 2048 pixels) installed at 50–130 mm distance from the samples was fixed on a separate stage and used to collect the two-dimensional diffraction signals. The samples were aligned to the specific diffraction planes, a series of diffraction images were recorded across the rocking-curve profiles at a step of ω angle 0.00025° (for 004) or 0.0005° (for 220). The measurements were performed at azimuthal angles of 0, 90, 180 and 270° along the surface normal (φ angle). The beam size at the sample location is 1.5 mm × 5 mm. Within the beam illuminating area, different indents can be covered.

The data analysis is critical, particularly for complex diffraction patterns, as it is not always straightforward due to the 'phase problem' in X-ray diffraction (Als-Nielsen, 2001). The codes for data analysis were made based on Matlab, and a flow chart of the codes is shown in Fig. 1. After background and geometry correction, the images were projected into the plane perpendicular to the sample surface. Maps of peak width (FWHM value, full width at half-maximum), peak position shift and integrated area under diffraction peaks were reconstructed by extracting data at each pixel from the XMDI images, from which the strain fields around defects and dislocations can be quantitatively evaluated.

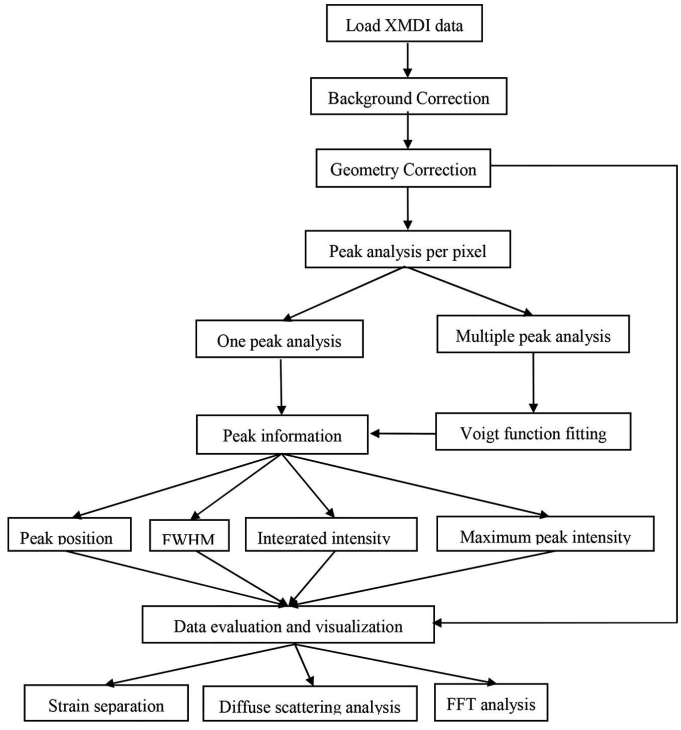

Figure 1
An overview flowchart of the code for XMDI data analysis.

3. Results and discussion

A line of Berkovich indents (from top to bottom, five 600 mN loads and five 500 mN loads) on the wafer were measured using XMDI. As shown in Fig. 2, a series of images recording the diffraction intensity were collected at 004 diffraction and at azimuthal angles of 0° (Fig. 2*a*) and 180° (Fig. 2*b*), respectively. The images show similar lateral symmetric 'bowl shaped' contrasts around each indent. A 600 mN indent marked in a rectangle of 150 µm × 130 µm in size was selected. Integrated intensity, peak-width and position-shift of the rocking curves were extracted at each pixel and the map of each component was plotted in Figs. 3(*a*)–3(*c*). A scanning electron microscopy image of the surface morphology around the indent is illustrated in Fig. 3(*d*) and a schematic of the Berkovich indenter, top and side views, is given in Fig. 3(*e*).

The integrated intensity of a diffraction peak is a measure of the electron density. Diffraction in defected crystal regions no longer obeys the dynamical theory, the diffraction intensity varies from a linear dependence to a quadratic dependence on the value of the structure factor, *i.e.* $\propto |F|^2$, according to the kinematic theory (Guinier, 1963). Therefore, a much enhanced contrast is observed in Fig. 3(*a*) around the indent in the background. The highlighted domain extends to a spatial field of ∼125 µm × 110 µm and is much larger and deeper than the indenter dimension on the wafer (∼10 µm × 2 µm). As X-rays have a large penetration depth (attenuation length 220 µm at 19 keV in silicon), the distribution under the indent is averaged in the beam propagation path in the sample and piled up in the longitudinal direction. As (004) are the planes parallel with the surface (001), the XMDI data collected at 004 diffraction contain mostly depth-dependent information, but modulated by the surface-distributed part because of the 13.9° incident angle.

The crystal quality is related to the peak width of diffraction. Most defects in a crystal cause a change of diffraction peak width, hence the peak-width map reflects largely the spatial distribution of defects. Fig. 3(*b*) shows a detailed peak-width map around the indent. The highest FWHM values (∼14.4 arcsec) are about twice of those in the perfect silicon crystalline regions. The highly defected bands 4–5 and 6–7 are from the zones underneath the indent and are oriented along the {111} crystal planes. It is ∼40 µm deep under the imprint of the indenter. Silicon is a brittle material and failure usually occurs along the {111} cleavage plane (Cook, 2006). Three regions marked as 1, 2 and 3 indicate defects near the surface around the indent, which are closely related to the triangular shape of the indenter (red triangle mark). A dark area, *i.e.* narrower peak width than that of the perfect substrate, of ∼20 µm lateral size around the indent, is visible above the mark 3. This can be due to the severe plastic deformation. This is the area in which phase transitions and large plastic deformations may occur and have been investigated by a variety of techniques (Jian, 2008). The measured rocking curves deviate significantly from the ideal Bragg condition because of the distortions; hence, narrower peak-width values were observed.

The map of peak position shift (shown in Fig. 3*c*) from the mean Bragg diffraction position corresponds to a measure of the local expansion or shrinkage of lattice parameters and, hence, a measure of the macroscopic strain field. Three large zones with warm colors (1, 2 and 3) are observed, symmetrically distributed around the indent, most probably resulting from the compression of the three triangular indenter side walls near the wafer surface. The shape effect of the triangular indenter is clearly seen from the map, and the strain and defect distribution is radially anisotropic. Zone 3 also contains a projection of the highly positive peak shifted area under the indent. The defected bands at 4–5 and 6–7 in Fig. 3(*b*) are shown as boundaries where the strain field changes sign in the depth dimension. This indicates that the lattice strains have been largely relaxed at this boundary. Deeper in the bulk (below 4–7), a light-blue broad band is shown, indicating a tensile strain field. It is ∼40 µm deep and ∼95 µm in lateral dimension. The two strain fields (above and below 4–7) have almost no peak broadening in Fig. 3(*b*).

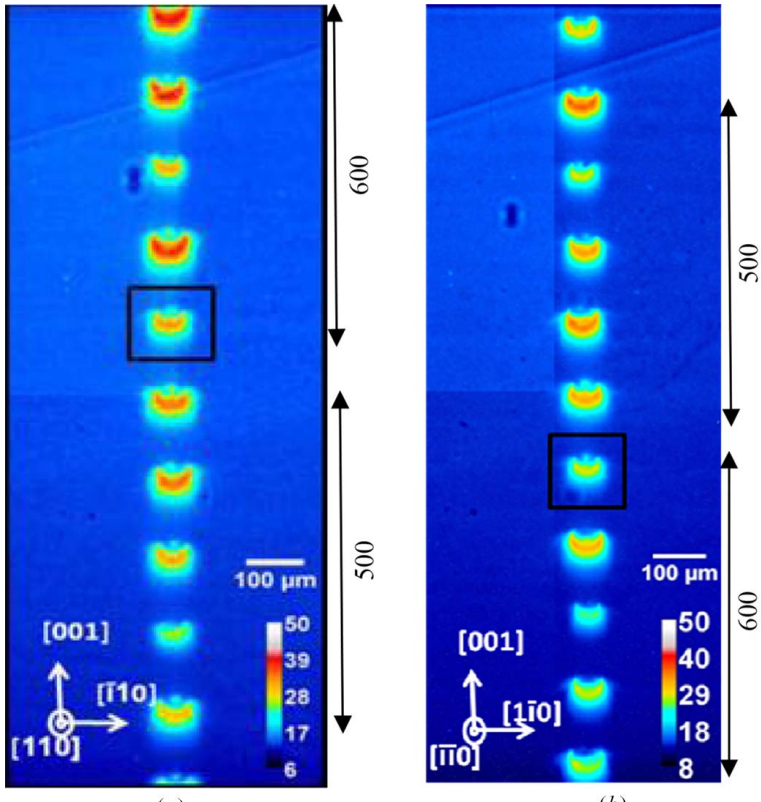

(*a*) (*b*)

Figure 2
Maps of integrated intensity of 004 diffraction in a line of Berkovich indents (from top, five 600 and five 500 mN loads) on the silicon wafer (001). XMDI data were collected at azimuthal angle 0° (*a*) and 180° (*b*). The same indent with 600 mN load is marked by a black frame in the two geometries.

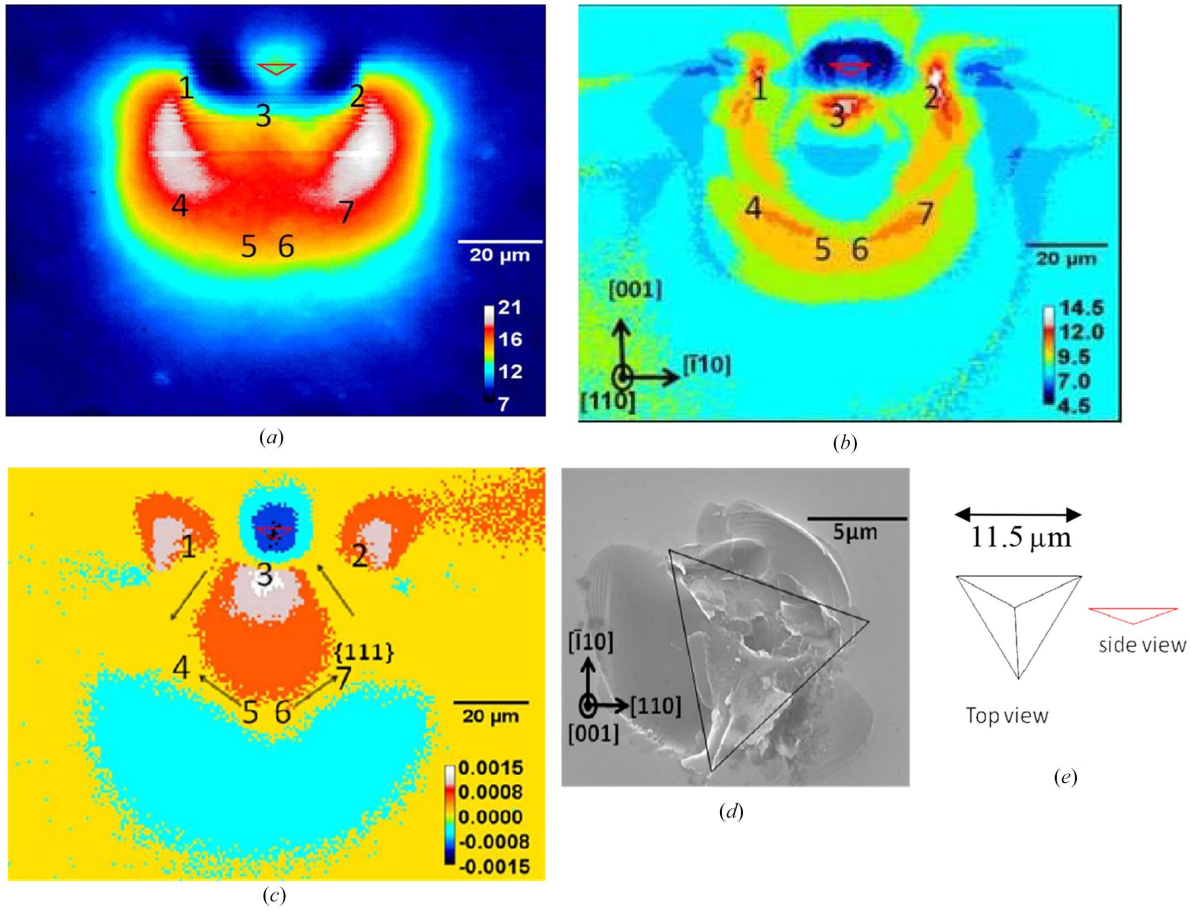

Figure 3
Maps of integrated intensity (*a*), peak width in arcsec (FWHM value) (*b*) and peak position shift in degree (*c*) of rocking curves around a 600 mN Berkovich indent in the silicon wafer. The data were extracted from XMDI images at the 004 diffraction and at azimuthal angle of 0°. (*d*) SEM image showing the surface morphology around the indent area. (*e*) Schematic of the indenter in top and side views. The indent is marked as a triangle in (*a*), (*b*) and (*c*) in side view. The arrows in (*c*) mark four {111} crystal planes. The marks 1–7 are explained in the text.

In imperfect crystals, the shift of the Bragg peak position corresponds to a crystal lattice change, *i.e.* lattice expansion (or contraction); however, it is also related to the tilt of the crystal plane (mosaicity). The two parameters can be further separated. The rocking curve of a diffraction of a crystal plane can be written as equation (1) (Bowen & Tanner, 1998),

$$\Delta\omega_{\rm B} = -\tan\omega_{\rm B}\left(\Delta d/d\right) \pm \Delta\varphi, \qquad (1)$$

$$\Delta d/d = \frac{1}{2}(\Delta\omega_0 + \Delta\omega_{180})\cot\theta_{\rm B}, \qquad (2)$$

$$\Delta\varphi = \frac{1}{2}(\Delta\omega_0 - \Delta\omega_{180}), \qquad (3)$$

where $\omega_{\rm B}$ is the Bragg angle, $\Delta\omega_{\rm B}$ is the local peak position shift from $\omega_{\rm B}$, $\Delta\varphi$ is the tilt of the crystal plane and d is the lattice parameter. By measuring XMDI at a pair of complementary azimuthal angles (ω_0 and ω_{180}), the parts due to $\Delta d/d$ and $\Delta\varphi$ can be separated using equations (2) and (3). It should be noted that the beam paths at the two complementary angles are not exactly identical because of the different illuminating volume in the beam path where X-rays penetrate. However, for a statistically homogeneous medium, the ensemble-averaged intensities over the crystal states for a given value of the source position are equal in the two geometries for a large extent of the X-ray plane wave on the surface. The average is obtained either *via* an ensemble average over crystal states or over entry points on the sources (Wilkins, 1981). In general, two types of strains can be distinguished: (i) micro-strain, varying from one grain or defect to another on a microscopic scale; (ii) macro-strain, where the stress is uniform over large distances. Usually micro-strain is non-uniform and it causes a broadening of diffraction; while macro-strain is homogeneous, meaning that all lattices are strained by the same amount, which in diffraction causes a peak shift. Structural defects induce local non-uniform strain within a crystal, the strength of strain obviously being greater at distances close to the actual defect. In this case, equations (1)–(3) can be also adopted, but the term $\Delta\theta$ is not the peak position shift, but the peak broadening caused by the non-uniform strain. The broadening is usually a convolution of instrumental resolution, grain size, local strain and all type of defects (Cullity & Stock, 2001).

Figs. 4(*a*) and 4(*b*) show the separate $\Delta d/d$ and $\Delta\varphi$ maps of the same indent. The map of $\Delta d/d$ is directly associated with the macroscopic stress and, hence, the lattice strain. In the

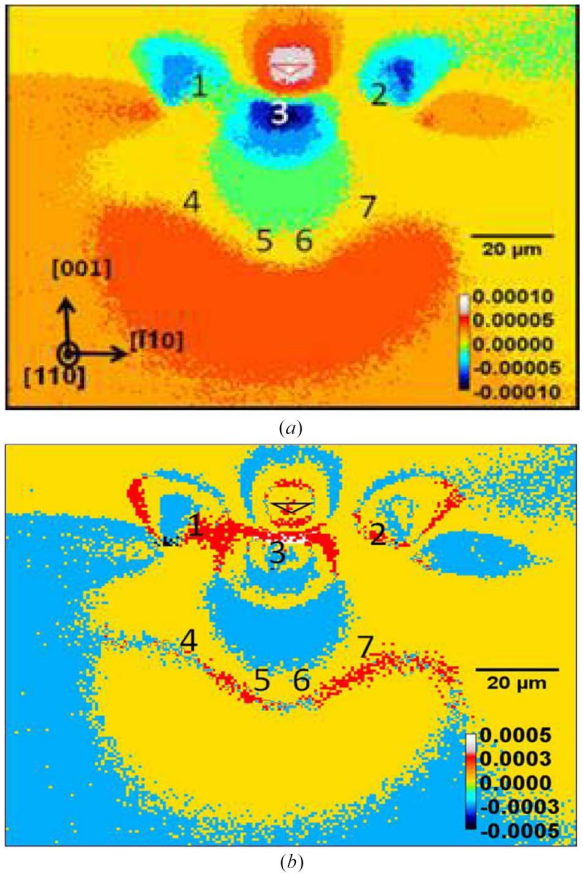

Figure 4
(*a*) Separated $\Delta d/d$ map and (*b*) $\Delta\varphi$ (°) map of the same indent shown in Fig. 2.

separated maps, it is seen that lattice expansion (contraction) and tilt coexist, and present similar spatial patterns. The difference is that the crystal plane inclination usually occurs at the boundaries of the strain field pads, while the lattice parameter variation spreads over a continuous smooth field. The crystal tilt or mosaicity is mostly observed around 1–3, which is much surface distributed. It can also be noticed that the $\Delta d/d$ map gives a higher color contrast which indicates that $\Delta d/d$ is dominant at this measuring condition. As a direct measure of lattice change, the $\Delta d/d$ map presents a detailed evaluation of strain and stress field. Similarly the broad compressive and tensile bands are clearly identified. These almost defect-free strain bands may imply an elastic strain character, which was induced by the plastically deformed region directly under the indent contact. The highest compression area is found located at ∼20 μm deep (mark 3) below the indenter impression. It is located at the plastic deformation zone with a lattice contraction rate of $\Delta d/d \simeq 1 \times 10^{-4}$.

Compared with uniform deformation, gradient-dominant deformation at the microscale can consistently show remarkable strengthening effects of materials (Haque & Saif, 2003). Strain gradient plasticity models have been proposed (Fleck *et al.*, 1994; Stölken & Evans, 1998) based on the hypothesis that stress at any points depends not only on the strain, but also on the strain gradient at that point. It is very critical to quantitatively measure and map the strain gradient in the bulk of materials.

The quantitative characterization of the strain field gradients induced by indentation can be easily made from the XMDI maps. As shown in Fig. 5, data along three vertical and horizontal profiles were extracted from the $\Delta d/d$ map. The gradients were estimated from the slope along the strain profiles. The central vertical line at 70 μm (V70) crosses from the plastically deformed area (grey) to the deeper compressive zone (dark blue); a maximum $\Delta d/d$ gradient of 1.6×10^{-5} μm^{-1} is observed at ∼20 μm under the indent. It is located at the boundary of these two zones. This local gradient may cause failures as the wafer undergoes a large stress. The H18 line also shows large gradients as it crosses the indented area; the gradient on both side of the central profile peak are 1.2×10^{-5} μm^{-1} and -8.8×10^{-6} μm^{-1}, respectively. The crystal lattice variation induces a macroscopic stress in the wafer. In the ⟨001⟩ directions the Young's modulus is a constant, ∼130 GPa; the uniaxial stress should have a similar

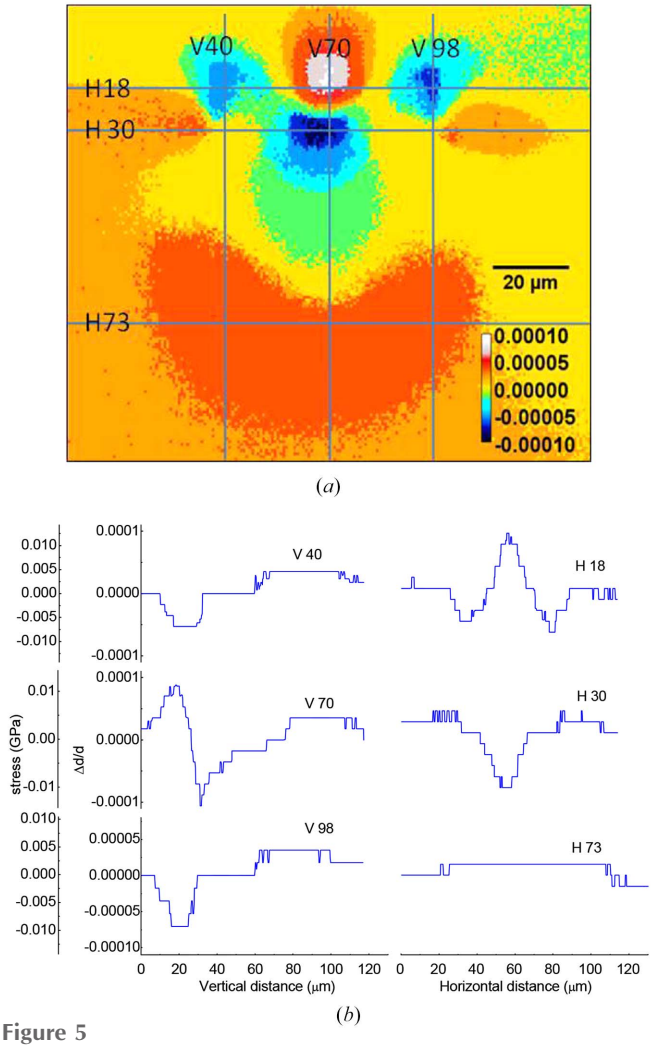

Figure 5
(*a*) $\Delta d/d$ map of the same indent as in Fig. 2, meshed with three vertical and three horizontal profile lines. The marks refer to the distance in micrometers from the origin (top left) of the map. (*b*) $\Delta d/d$ profiles along the three vertical (V) and three horizontal (H) lines. The stress with respect to $\Delta d/d$ is also labeled in the ordinate axis.

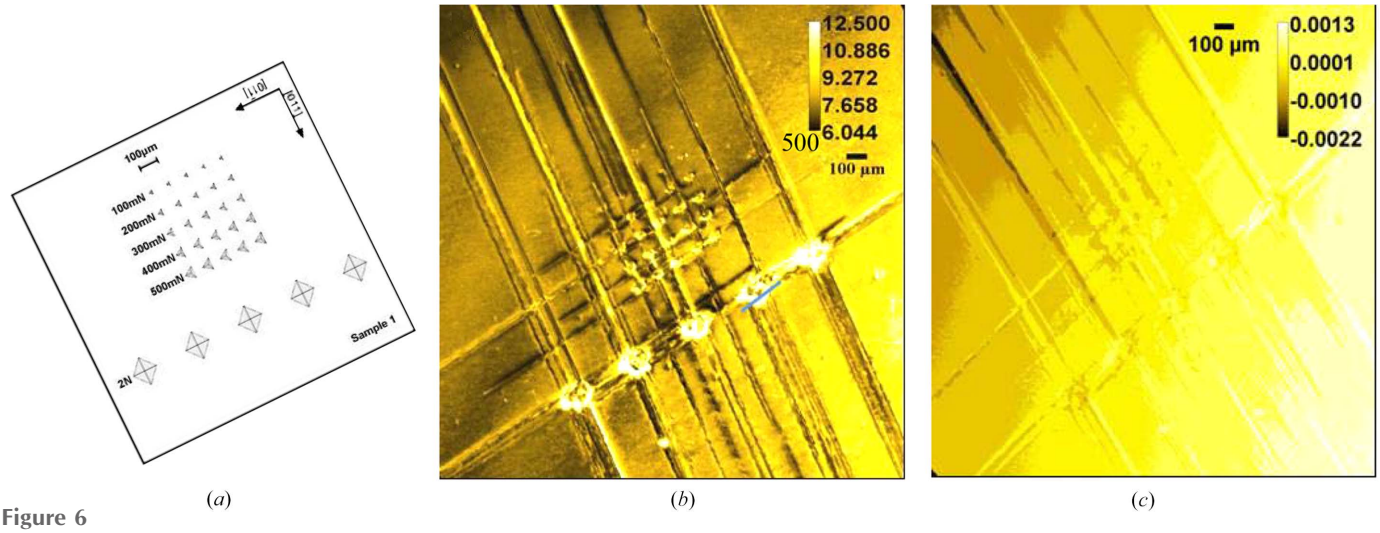

(*a*) (*b*) (*c*)

Figure 6
A schematic of indent arrays on the silicon wafer, annealed at 1273 K (*a*). Indents are made with a Vickers or Berkovich indenter with a series of loads. The upper five indents are 2 N load made by a Vickers tip; the 5 × 5 array is from 100 mN to 500 mN loads made by a Berkovich indenter. (*b*) FWHM and (*c*) peak position-shift maps of the indented and annealed silicon wafer, extracted from the XMDI data collected from the 220 diffraction in transmission mode. A profile line is drawn across the indent in (*b*).

distribution as the strain field but modulated with a constant in 130 GPa, as shown in Fig. 5.

Fig. 6 shows the full-field-of-view of the peak width (*b*) and peak position shift (*c*) of XMDI maps measured at 220 diffraction and Laue transmission mode of the indented wafer slowly annealed at 1273 K. A diagram of the indentation array containing a five 2 N Vickers indent line (large prism) and a 100–500 mN Berkovich indent array (small triangle) is illustrated in Fig. 6(*a*). Some crossed stripes are clearly observed oriented along the indent array, spreading all over the wafer surface. Highly structural defected zones generally have a high contrast in the peak-width map because of the broadening effect of defects to the diffraction peaks. It is clearly seen that defects can be well probed and characterized by the peak-width map of XMDI. The dislocation lines and slip bands can be resolved and are clearly indentation load dependent. Each stripe of the slip band is a combination of a certain number of parallel dislocation lines. Similar patterns have also been observed by *in situ* X-ray topography experiments (Danilewsky *et al.*, 2011) of the same sample series and ascribed to the accumulation of oriented dislocation lines. Upon annealing at high temperature, the dislocation lines have developed from individual, separate bands as seen in the above separate peak width maps, into a well connected dislocation network spreading over the whole wafer. It is seen that these dislocation slip bands are crossed at each indent node in the indentation array and oriented along $[01\bar{1}]$ and [011], being perpendicular to each other. The larger indentation loads generate a larger highlighted field. The strain and defect field is ∼45 μm in dimension and has a FWHM value of 6.9–15 arcsec for each 100 mN-loaded indent, and it extends up to ∼180 μm and 14–122 arcsec for the 2 N-loaded indent.

Fig. 6(*c*) presents the respective peak position shift map. In contrast to the peak-width map; the contrast of each array is rather light compared with the perfect crystal, which indicates a small shift of the diffraction peak. As the peak shift mainly reflects the lattice parameter variation or inclination, and hence the strain field or mosaicity, it clearly indicates that the slow annealing treatment has largely released the elastic strain field in the wafer sample.

In a quantitative evaluation, the rocking-curve data at each pixel over a profile line crossing a 2 N indent edge shown in Fig. 6(*b*) (blue line) were extracted from the XMDI data, and peak fitting was performed. As shown in Fig. 7, the typical

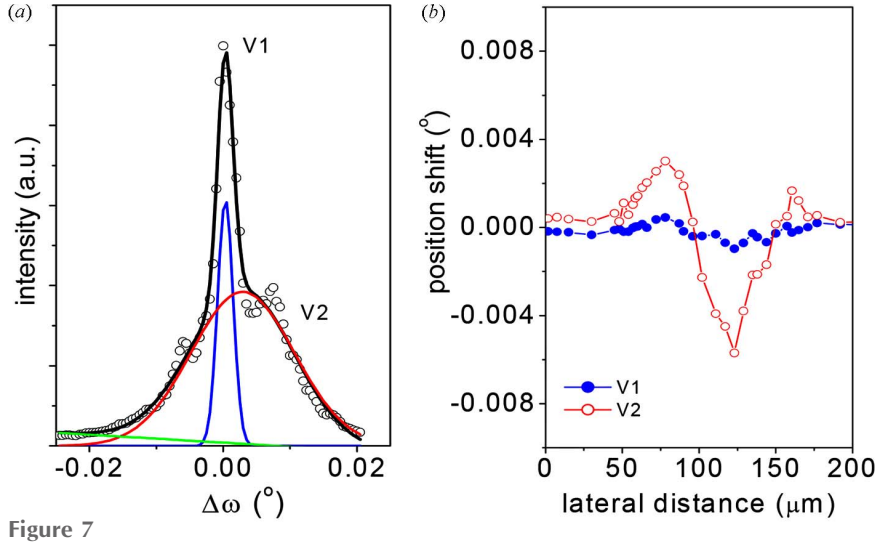

Figure 7
(*a*) Fitting of a rocking-curve profile with two pseudo-Voigt functions and one linear function in a pixel. (*b*) Plots of peak position shift of the two fitting functions along the blue profile line in Fig. 6(*b*).

rocking curve at a typical pixel shows a sharp peak imposed on a broadened peak. In a simple model, two pseudo-Voigt functions and one linear function were employed for the fit. In the fit, the peak width of the shape component was kept constant. In a first-order approximation, the two-Voigt components can simply represent the distorted and perfect silicon volume within a pixel. Fig. 7(*b*) shows the peak position shift plot of the two Voigt components along the profile line. The sharp component (V1) is nearly constant, whereas the broadened component (V2), representing the deformed region with strain and defects, shows a deep valley at the center of the indenter impression surrounded by the two protruding edges on both sides of the indent. This is consistent with the Raman results (Allen *et al.*, 2010), in which a similar profile has been observed, and explained as a tensile zone under the center of the slip bands and two neighboring compressive areas under the side wall of the indenter. The strained field is estimated to be ∼150 µm in the lateral dimension.

Previous reports (Tachi *et al.*, 2002; Oliver & Pharr, 1992; Domnich & Gogotsi, 2002) have mostly focused on the plastically deformed zones under the indenter, where multiphase, amorphization and phase transition can occur, and can play a critical role in the mechanical properties and semiconductor processing. For the first time, the strain field far beyond this deformed zone has been observed and investigated in a quantitative way in the bulk of silicon wafers. The advantage for the synchrotron-radiation-based XMDI method is clearly demonstrated from the above analysis. It can penetrate the sample with a depth that can be varied by the X-ray photon energies and measuring geometric mode. It also presents a relatively large field of view (several cm^2) that allows for a more reliable evaluation of the whole wafer samples. In combination with a high-resolution CCD detector, the spatial resolution is in the scale of a pixel size, *i.e.* one or several micrometers. The image data were collected in one shot. In addition, the selection of reflection planes provides different geometries for strain mapping. The map measured at 004 diffraction, as these are the planes that are parallel with the (001) surface of wafers, is more depth dependent; while the measurement at 220, by projection, is more related to surface distribution. In a series of images, the XMDI technique presents a material characterization at two distinct levels: the crystal lattice measurements at the ångström or nanometer level and strain, defect field map at the microscale level, with the help of the short wavelength of the X-ray probe and high-resolution area detector. The two-level structural information is complementary and is of significant importance for the investigation of electronic, mechanical or transport properties of crystalline materials. At last the XMDI method is quantitative, the evaluation of rocking-curve data at each pixel by peak fitting or peak analysis presents high-contrast, high-resolution field of view; in contrast, the X-ray topography is limited to resolving the details of the as-received silicon wafers without any annealing treatment (Danilewsky *et al.*, 2011).

For engineers manufacturing semiconductors, finding optimal working conditions and minimizing bulk damage in silicon wafers remain as great challenges. The XMDI method provides a quantitative characterization of defects and strain fields around indents, and compares well with earlier FEM simulations (Ivashchenko *et al.*, 2008) and micro-Raman spectroscopy (Bowen & Tanner, 2010). Because of the high-energy X-ray photons employed here, this technique gives much deeper bulk information compared with micro-Raman spectroscopy. Various parameters with respect to a Bragg diffraction peak can be used for a complementary evaluation of strain and defect fields induced by indentation, therefore, XMDI presents a more detailed and more sophisticated map of defects and strain field compared with the simulations by FEM.

It should also be added that XMDI is much faster than previous microbeam diffraction which requires fairly focused X-ray beams and stepwise scanning of samples (Rogan *et al.*, 2003; Murray *et al.*, 2003). In XMDI, the image data are taken in one shot; therefore, it is more straightforward and can be used for *in situ* investigations.

4. Conclusions

In summary, the XMDI method using synchrotron radiation was employed to investigate the indent-induced strain and defect distribution in silicon wafers. The extracted FWHM values, peak position shift and integrated intensity of diffraction rocking curves were mapped to present a quantitative characterization of the two-dimensional distributions of strain fields and defect locations. The large compressive and tensile strain zones were mapped out below the plastically deformed zone under the indent. The distribution is about 100 µm wide and 100 µm deep in the wafer for a 600 mN load indent, and is dependent on indenter shape and crystal anisotropy. From a series of XMDI measurements at different azimuthal angles, the maps corresponding to lattice compression (or tension) and lattice tilt (mosaicity) were separated. It was found that at the 004 reflection of XMDI the depth-dependent strain fields are dominant in the measured strain field. While at the 220 reflection, the XMDI is mostly surface plane oriented. Upon annealing, the strain and defects can be much released. This implies an elastic strain nature. The plastically deformed zone under the indenter impression is shown as a black spot in XMDI because of numerous defects and distortions; it generates a maximum strain and stress gradient. This technique shows potential for the nondestructive analysis and monitoring of local strain fields and defect locations in semiconductor industrial applications.

Acknowledgements

The project is financially supported by EU-FP7 project (No. 216382 SiDAM). We would like to thank T. Liu, P. Reischig, D. Hänschke, P. Vagovic, F. Xu (Karlsruhe Institute of Technology, Karlsruhe, Germany), D. K. Bowen, B. K. Tanner (Durham University, UK) and P. Yang (Singapore Synchrotron Light Source) for helpful discussions. The indented silicon samples were prepared by E. Gorostegui-Colinas,

J. Garagorri, M. R. Elizalde (Centro de Estudios e Investigaciones Tecnicas de Gipuzkoa).

References

Allen, D., Wittge, J., Zlotos, A., Gorostegui-Colinas, E., Garagorri, J., McNally, P., Danilewsky, A. N. & Elizalde, M. R. (2010). *Nucl. Instrum. Methods Phys. Res. B*, **268**, 383–387.

Als-Nielsen, J. (2001). *Elements of Modern X-ray Physics.* New York: John Wiley and Son.

Bouhassoune, M. & Schindlmayr, A. (2010). *Phys. Status Solidi C*, **7**, 460–463.

Bowen, D. K. & Tanner, B. K. (1998). *High Resolution X-ray Diffractometry and Topography.* London: Taylor & Francis.

Bowen, D. K. & Tanner, B. K. (2010). *Nucl. Instrum. Methods Phys. Res. B*, **268**, 3–4.

Cook, R. F. (2006). *J. Mater. Sci.* **41**, 841–872.

Cullity, B. D. & Stock, S. R. (2001). *Elements of X-ray Diffraction.* Upper Saddle River: Prentice Hall.

Danilewsky, A., Wittge, J., Croell, A., Allen, D., McNally, P., Vagovič, P., dos Santos Rolo, T., Li, Z., Baumbach, T., Gorostegui-Colinas, E., Garagorri, J., Elizalde, M. R., Fossati, M., Bowen, D. K. & Tanner, B. (2011). *J. Cryst. Growth*, **318**, 1157–1163.

Danilewsky, A., Wittge, J., Hess, A., Cröll, A., Allen, D., McNally, P., Vagovič, P., Cecilia, A., Li, Z., Baumbach, T., Gorostegui-Colinas, E. & Elizalde, M. R. (2010). *Nucl. Instrum. Methods Phys. Res. B*, **268**, 399–402.

Domnich, V. & Gogotsi, Y. (2002). *Rev. Adv. Mater. Sci.* **3**, 1–36.

Ericson, F. S., Johansson, S. & Schweitz, J.-K. (1988). *Mater. Sci. Eng. A*, **105–106**, 131–141.

Fleck, N. A., Muller, G. M., Ashby, M. F. & Hutchinson, J. W. (1994). *Acta Metall. Mater.* **42**, 475–487.

Gilman, J. (2008). *J. Phys. D*, **41**, 074020.

Guinier, A. (1963). *X-ray Diffraction.* San Francisco: W. H. Freeman.

Haque, M. A. & Saif, M. T. A. (2003). *Acta Mater.* **51**, 3053–3061.

Helfen, L., Myagotin, A., Pernot, P., DiMichiel, M., Mikulík, P., Berthold, A. & Baumbach, T. (2006). *Nucl. Instrum. Methods Phys. Res. A*, **563**, 163–166.

Ivashchenko, V. I., Turchi, P. E. A. & Shevchenko, V. I. (2008). *Phys. Rev. B*, **78**, 035205.

Jacobsen, R., Andersen, K. N., Borel, P. I., Fage-Pedersen, J., Frandsen, L. H., Hansen, O., Kristensen, M., Lavrinenko, A. V., Moulin, G., Ou, H., Peucheret, C., Zsigri, B. & Bjarklev, A. (2006). *Nature (London)*, **441**, 199–202.

Jian, S. R. (2008). *Nanoscale Res. Lett.* **3**, 6–13.

Khayyat, M. M., Banini, G. K., Hasko, D. G. & Chaudhri, M. M. (2003). *J. Phys. D*, **36**, 1300–1307.

Lübbert, D., Baumbach, T., Härtwig, J., Boller, E. & Pernot, E. (2000). *Nucl. Instrum. Methods Phys. Res. B*, **160**, 521–527.

Lübbert, D., Baumbach, T., Mikulik, P., Pernot, P., Helfen, L., Köhler, R., Katona, T. M., Keller, S. & DenBaars, S. P. (2005). *J. Phys. D*, **38**, A50–A54.

Lübbert, D., Ferrari, C., Mikulík, P., Pernot, P., Helfen, L., Verdi, N., Korytár, D. & Baumbach, T. (2005). *J. Appl. Cryst.* **38**, 91–96.

Mikulik, P., Lübbert, D., Korytár, D., Pernot, E. & Baumbach, T. (2003). *J. Phys. D*, **36**, 74–78.

Murray, C. E., Noyan, I. C., Mooney, P. M., Lai, B. & Cai, Z. (2003). *Appl. Phys. Lett.* **83**, 4163–4165.

Oliver, W. C. & Pharr, G. M. (1992). *J. Mater. Res.* **7**, 1564–1583.

Rogan, R. C., Tamura, N., Swift, G. A. & Üstündag, E. (2003). *Nat. Mater.* **2**, 379–381.

Stölken, J. S. & Evans, A. G. (1998). *Acta Mater.* **46**, 5109–5115.

Tachi, M., Suprijadi, M. T., Arai, S. & Saka, H. (2002). *Philos. Magn. Lett.* **82**, 133–139.

Wilkins, S. W. (1981). *Philos. Trans. R. Soc. A*, **299**, 275–317.